nature electronics

Article

https://doi.org/10.1038/s41928-023-01029-4

Spin-acoustic control of silicon vacancies in 4H silicon carbide

Received: 2 September 2022

Accepted: 10 August 2023

Published online: 21 September 2023

Check for updates

Jonathan R. Dietz[1,3], Boyang Jiang[2,3], Aaron M. Day[1], Sunil A. Bhave[2] ✉ & Evelyn L. Hu[1]

Bulk acoustic resonators can be fabricated on the same substrate as other components and can operate at various frequencies with high quality factors. Mechanical dynamic metrology of these devices is challenging as the surface information available through laser Doppler vibrometry lacks information about the acoustic energy stored in the bulk of the resonator. Here we report the spin-acoustic control of naturally occurring negatively charged silicon monovacancies in a lateral overtone bulk acoustic resonator that is based on 4H silicon carbide. We show that acoustic driving can be used at room temperature to induce coherent population oscillations. Spin-acoustic resonance is shown to be useful as a frequency-tunable probe of bulk acoustic wave resonances, highlighting the dynamical strain distribution inside a bulk acoustic wave resonator at ambient operating conditions. Our approach could be applied to the characterization of other high-quality-factor microelectromechanical systems and has the potential to be used in mechanically addressable quantum memory.

Acoustic control of semiconductor defect spins can complement magnetic control in sensing and quantum information processing applications[1]. Acoustic driving can, for instance, manipulate the full ground-state spin manifold of several defect systems with a spin greater than spin-1/2 (refs. 2–4). Hybrid systems that employ both acoustic and magnetic control of defect spin states provide a means to transduce spin signals and can facilitate the integration of spin systems with more conventional technology[5]. Silicon carbide (SiC) is an ideal material platform for developing such a hybrid quantum system as it has already been used to create high-performance optical, acoustic and electronic devices[6–9].

The acoustic control of defect spins is also useful for the metrology of microelectromechanical systems (MEMS)[2,10,11]. The metrology of diamond-based sensors has already been demonstrated, but metrology using defects in SiC—which hosts several strain-sensitive spin active defects—remains a desirable advance towards commercial applications[12]. A variety of techniques can be used to analyse the performance of radio-frequency (RF) MEMS resonators and filters, including laser Doppler vibrometry and white-beam X-ray tomography[13–15]. However, these have a limited ability to probe the actual distribution of strain within the resonator material. Such knowledge is critical in optimizing resonator design as well as improving the quality factor (Q) and power handling. As a result, a depth-sensitive, room-temperature metrology approach such as optically detected spin-acoustic resonance (ODSAR)-based MEMS characterization is desirable.

Silicon monovacancies are a long-studied defect system in SiC as a spin–photon interface[16–18]. The singly negatively charged k-site silicon monovacancy (V_{Si}^{-}) is particularly attractive due to its bright, near-infrared optical transition, often labelled V2 in the literature, and its spin-3/2 ground-state manifold that can be manipulated through its room-temperature ODSAR[4]. It is desirable to monitor V_{Si}^{-} within acoustic resonators, where most of the mechanical strain energy is stored in a single-crystal material rather than in the piezoelectric transducer. Surface acoustic wave cavity resonators satisfy this criterion, and a Gaussian surface acoustic wave resonator has been used to drive spin resonances in silicon vacancy and divacancy spin ensembles in 4H-SiC (refs. 2,19). However, in this case, the mechanical strain energy is concentrated near the resonator surface, making the surface acoustic wave cavities' Q values and frequencies susceptible to changes in surface conditions[20]. In addition, the coherence of colour centres

[1]John A. Paulson School of Engineering and Applied Sciences, Harvard University, Cambridge, MA, USA. [2]OxideMEMS Lab, Purdue University, West Lafayette, IN, USA. [3]These authors contributed equally: Jonathan R. Dietz, Boyang Jiang. ✉e-mail: bhave@purdue.edu

https://doi.org/10.1038/s41928-023-01029-4

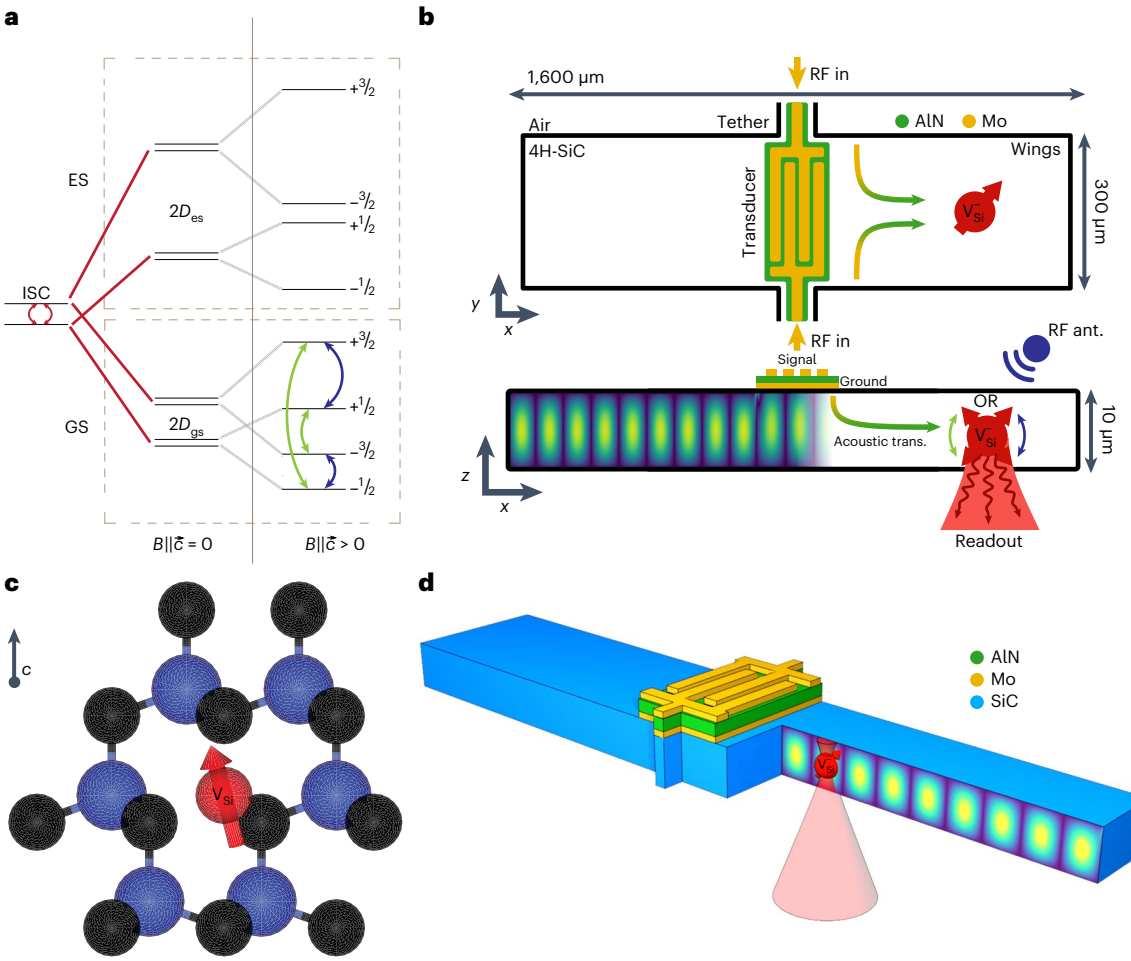

Fig. 1 | Defect and device structure. a, Electronic structure of V_{Si}^- with magnetically allowed and magnetically forbidden but acoustically allowed transitions labelled in blue and green, respectively. Spin polarization is created through ground-state (GS) transduction and then readout by the fluorescence difference between spin manifolds resulting from different non-radiative decay rates and intersystem crossing (ISC) from the defects' optically excited state (ES). The spin resonances are Zeeman shifted into resonance with the LOBAR with a *c*-axis-oriented magnetic field (*B*). **b**, Schematic of the suspended LOBAR device transduction and spin control. Interdigital molybdenum (Mo) electrodes excite an aluminium nitride (AlN) piezoelectric layer that converts the input RF photons into phonons, which acoustically transduce a V_{Si}^- spin shown by a yellow-to-green arrow to observe ODSAR. Alternatively, the spin can be magnetically transduced by a nearby suspended RF antenna to observe ODMR. The spin is then readout with an excitation laser focused onto the backside of the resonator. For reference, an FEM-simulated strain distribution of the shear strain of an A_0 Lamb wave mode is shown. **c**, Crystallography of the *k*-site V_{Si}^- (V2) defect centre, with the nearest-neighbour carbon and silicon atoms (shown in black and blue, respectively). The *c* axis(0001) is labelled. **d**, Alternate representation of the experimental schematic shown in **b**.

themselves is also sensitive to surface conditions and the presence of stray electric fields, making it desirable to develop devices that make emitters locally addressable in the bulk material, a goal that bulk acoustic resonators enable[21,22]. Additionally, bulk acoustic resonators enable rapid mechanical pulsing, enabling the direct observation of mechanically driven coherent population oscillations[22].

In this Article, we report the acoustically mediated spin control of naturally occurring silicon monovacancies (V_{Si}^-) in a high-*Q* lateral overtone bulk acoustic resonator (LOBAR) fabricated in high-purity semi-insulating 4H-SiC. We use LOBARs in our study, which preserve strain in the entire resonator body rather than on the surface alone. LOBARs are overtone acoustic wave resonators, where the acoustic cavity length (and hence the resonances) is controlled by the lateral, lithographically defined extent of the resonator. SiC LOBARs have been demonstrated with mechanical *Q* values of 3,000 to 20,000 with frequencies ranging from megahertz to gigahertz[23,24]. We study the spatial characteristic of the acoustic coupling of LOBARs to an ensemble of silicon monovacancies. We demonstrate spatial, directional and frequency strain sensitivity, and show the coherent acoustic control of silicon monovacancies in the SiC. Our approach can enable high-spatial-resolution mapping of strain inside a MEMS resonator, and lays the foundation for the direct integration of spins into a wafer-scale material platform for quantum information processing.

Measurement of ODSAR

In our LOBAR devices, V_{Si}^- is present as a naturally occurring, intrinsic point defect, giving us the ability to characterize the coupling between its acoustic mode and the V_{Si}^- ground-state spin (Fig. 1a). To unequivocally demonstrate spin-acoustic coupling in our devices, we alternately apply strain to the ensemble with a differentially driven acoustic resonance via interdigital electrodes at its 89.5 MHz flexural mode, which is compared with magnetic driving via a nearby suspended RF antenna (Fig. 1b). Spin-3/2 defects have a spin–strain coupling Hamiltonian[10,11,25,26]:

$$H_\epsilon = \Xi \sum_{ij} h_{ij} \epsilon_{ij} S_i S_j, \quad (1)$$

https://doi.org/10.1038/s41928-023-01029-4

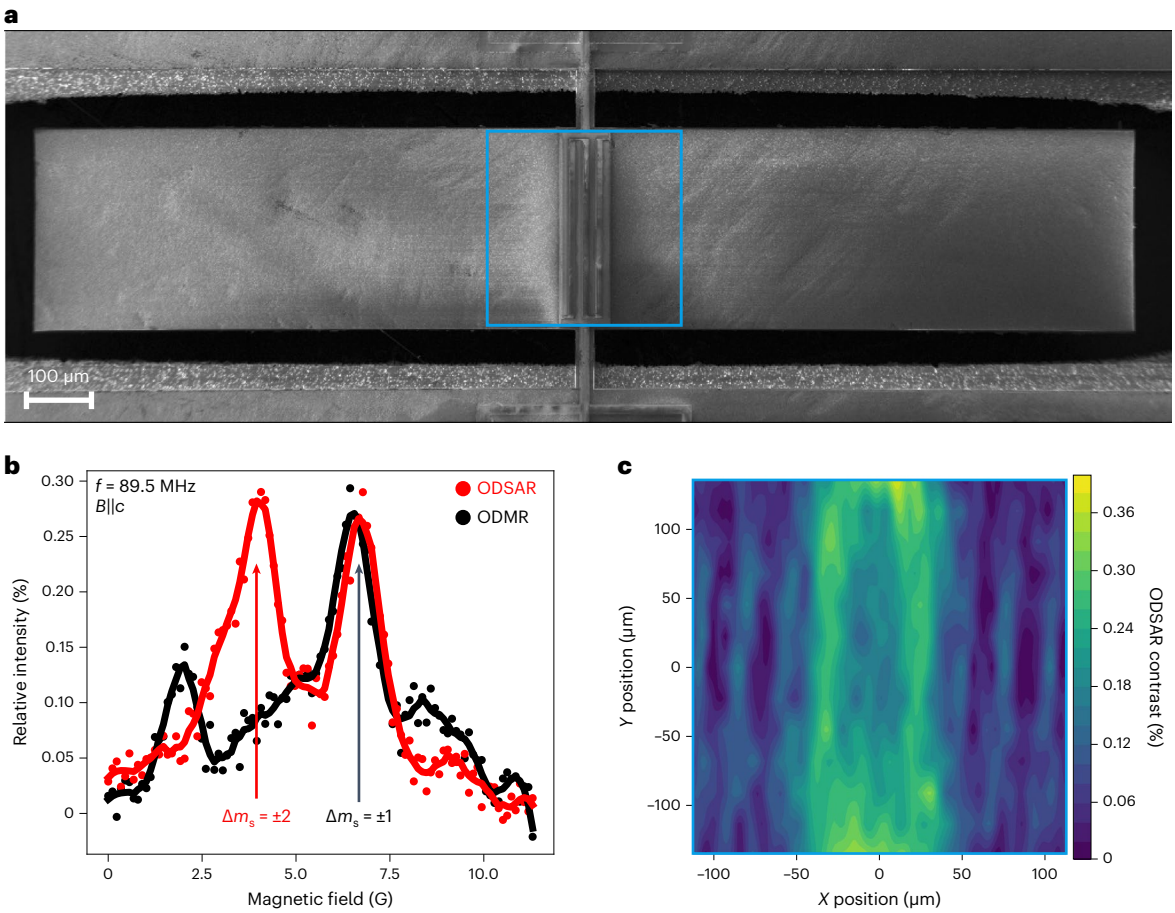

Fig. 2 | Spin-acoustic resonance mapping. a, Field-emission scanning electron microscope image of the LOBAR device measured in this experiment. **b**, Comparison of spin resonance driven at 89.5 MHz with an RF antenna (Fig. 1b, ODMR) against the LOBAR's transducer (ODSAR), showing clearly distinguishable peaks associated in energy with spin-1 magnetically allowed transition and a spin-1 and spin-2 acoustically allowed transitions. **c**, XY raster over the area marked in **a**, showing the characteristic of fringes of the flexural modes of the LOBAR device with the $\Delta m_s = 2$ transition.

where Ξ is the interaction strength, h_{ij} is the strain-coupling tensor from the V_{Si}^- $C3v$ symmetry, ϵ_{ij} is the Cartesian strain and S are the spin-3/2 spin matrices. We perform our measurements by tuning the frequency of the ground-state spin resonances with a magnetic field oriented parallel to the z axis of the resonator and c axis of the SiC (Fig. 1b). In this orientation, $\Delta m_s = \pm 1$ is driven by the $(\epsilon_{xx} - \epsilon_{yy})$, ϵ_{xy}, ϵ_{xz} and ϵ_{yz} terms and $\Delta m_s = \pm 2$ is entirely driven by the ϵ_{xy} and ϵ_{yz} terms[10]. We then collect the differential fluorescence of the k-site V_{Si}^- (Fig. 1c), from 900 to 1,150 nm, to measure the ODSAR. We focus our initial analysis on the asymmetric flexural A_0 Lamb wave mode of the LOBAR, since it has a higher piezoelectric coupling coefficient k_t^2, and thus, greater energy is transferred from the piezoelectric transducer to the SiC[27].

In our analysis, we differentiate between regions of the device shown in Figs. 1b and 2a: the transducer, where the Mo–AlN–Mo piezotransducer covers the SiC resonator; the wings, where the SiC is free of the transducer; and the tethers, where the bar is connected to the substrate. To improve the signal-to-noise ratio, a large pinhole of 50 μm is employed, which ensures that the confocal slice of the microscope averages over the full 10 μm device height during the measurements. From the ODSAR and optically detected magnetic resonance (ODMR) underneath the transducer shown in Fig. 2b, two peaks appear in the ODSAR spectrum, which correspond to $\Delta m_s = \pm 2$, which are not magnetically dipole allowed for the corresponding ODMR spectrum. Two-dimensional scans of the transducer and nearby wings reveal a characteristic fringe pattern when transduction is on resonance with one of the resonator's overtones (Fig. 2c). Supplementary Fig. 1 compares the power dependence of ODSAR for different regions of the device. We also note that the magnetic driving of the spin transition by stray RF fields from the interdigital electrode is suppressed because the SiC resonator is shielded from RF radiation by the presence of a ground plane underneath the signal electrodes having zero piezoelectric displacement current.

From Fig. 2c, it is clear that dynamic strain is highly concentrated in the direct vicinity of the transducer, with a slightly lower ODSAR contrast observed on the wings of the device. The flexural modes in the resonator address a smaller sub-ensemble of the defects probed by our confocal slice, resulting in a lower average strain over the depth slice. The higher dynamic strain under the transducer indicates that a larger ensemble is addressed by the acoustic waves, showing that spin dynamics underneath the transducer are driven by broadband piezoelectric actuation, whereas the dynamics on the wings are driven by acoustic standing waves that span the entire device. The increase in the ODSAR intensity near the tethers of the device quantitatively confirms that stress is concentrated between the suspended resonator and the surrounding substrate, providing a quantitative spatial measure of the acoustic loss in the LOBAR.

Metrology of different acoustic mode families with ODSAR

Next, we demonstrate that our technique is capable of spatially resolved metrology of strain in the bulk of the LOBAR by performing spatial confocal scans of the spin resonance intensity of mechanical modes.

https://doi.org/10.1038/s41928-023-01029-4

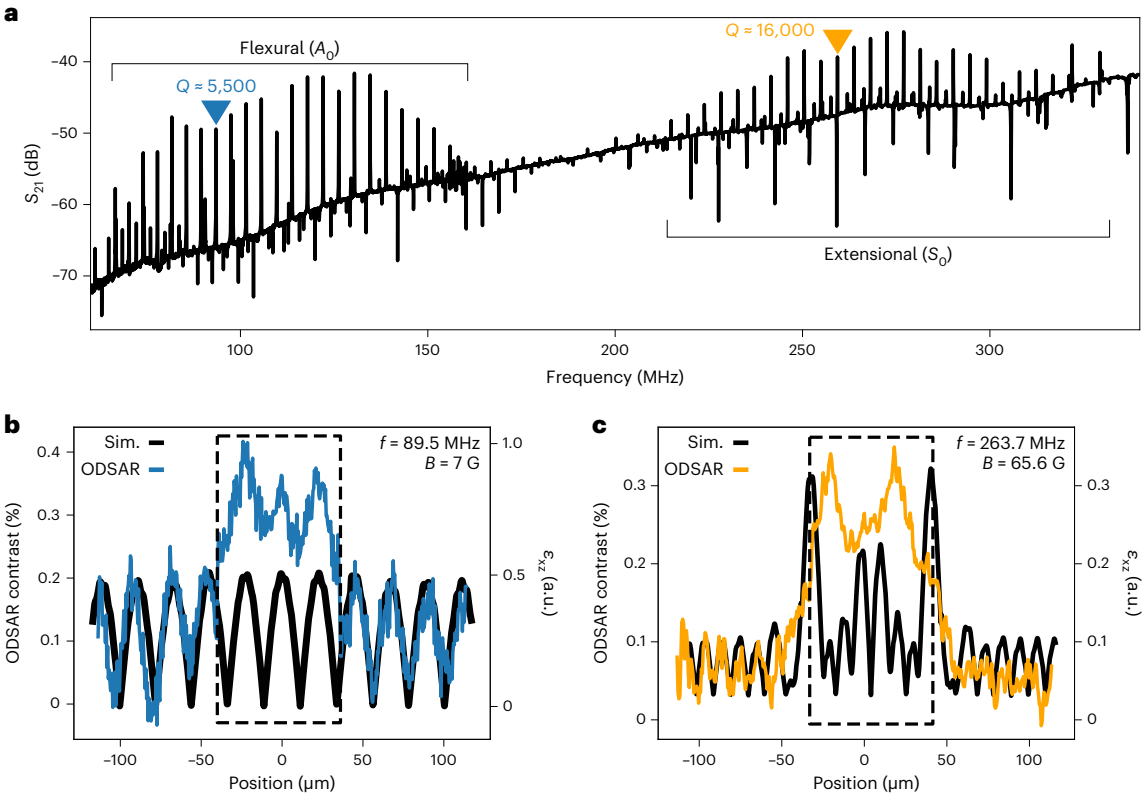

Fig. 3 | Spin-acoustic mode metrology. a, The S_{21} electrical properties of the resonator in air at room temperature, showing two overtone regions of flexural and extensional acoustic mode families, with the modes shown in **b** and **c** marked with their mechanical Q. **b**,**c**, Device linescan along the x axis of the device (Fig. 1b), showing the ODSAR intensity across the transducer and nearby wing regions of the device, compared with the simulated predictions for shear strain ϵ_{xz} in the 89.5 MHz flexural mode (**b**) and 260.7 MHz extensional mode (**c**) of the device. Underneath the transducer (dotted black box), ODSAR deviates from the simulation as a result of off-resonant piezotransduction.

From the electrical data shown in Fig. 3a, we observe the presence of two mode families corresponding to low-frequency flexural (A_0) and high-frequency extensional (S_0) modes, whose presence is predicted by finite element model (FEM) simulations. Flexural modes have out-of-phase longitudinal strain modes that result in a high overall shear strain. By contrast, extensional modes have high in-phase longitudinal strain but minimal shear strain, except for the shear strain introduced by symmetry breaking because of the transducer. In the subsequent work, we focus on $\Delta m_s = \pm 1$ transitions because they couple both shear and longitudinal strain and allow a comparison with the achievable Rabi rates with a standard magnetic drive (Fig. 1b).

ODSAR can also be used to study the depth-averaged device strain for different resonant mode families. We first identify two high-Q modes corresponding to the Lamb flexural A_0 and S_0 extensional mode families of the device (Fig. 3a and Supplementary Fig. 2). One-dimensional scans along the length of the resonator demonstrate a clearly differentiated spatial frequency and driving dynamics for the 89.5 MHz flexural and 263.7 MHz extensional modes of the resonator (Fig. 3b,c). With $\vec{B} \parallel \vec{c}$, the tuned $\Delta m_s = 1$ demonstrates a notably higher spin–strain coupling for high-shear-strain flexural modes. In the case of the flexural mode, this is confirmed, as the ODSAR shows excellent agreement with the shear strain of the resonator predicted by FEM simulation (Fig. 3b and Supplementary Figs. 3 and 5). By contrast, the extensional mode of the resonator is expected to have minimal shear strain, except for shear strain that is introduced by the symmetry-breaking effect of the transducer, which our scan confirms (Fig. 3c). We can also use our technique to probe the local acoustic dynamics introduced by etching asperities on the device (Supplementary Section 5). Local asperities cause strain localization, which leads to mechanical dissipation or a drop in Q. Such a spatially resolved strain localization is critical to identify 'Q-loss' regions and will provide feedback for improving the MEMS manufacturing technology.

Coherent acoustic control of silicon monovacancies

Finally, we demonstrate that ODSAR can be exploited for room-temperature coherent control, demonstrating that ground-state acoustic driving could be useful for state preparation as well as a resource for entanglement generation[28]. We first characterize the difference in the frequency-domain lineshape of the ODSAR (Fig. 4a). On the transducer, the ODSAR line is a broad 2 MHz resonance, whereas on the wings of the device, the line is narrowed, approaching the linewidth of mechanical resonance (Fig. 4b). Based on this insight, we compare Rabi oscillations directly underneath the transducer and on the wings with the same RF drive power, by initializing the spins with an initial laser pulse, measuring their photoluminescence (PL) followed by RF excitation at acoustic resonance with a varying pulse length and subsequently measuring the PL (Fig. 4c). The relative population difference from an undriven ensemble is inferred from the relative intensity between the initial and final PL measurements: $\mathrm{RI} = \frac{\mathrm{PL_f}}{\mathrm{PL_i}}$ (Fig. 4d). Under the wings, spins oscillate at 2.0 ± 0.2 MHz, compared with spins under the transducer that oscillate from off-resonant piezotransduction at 1.2 ± 0.2 MHz. This result contrasts the measurement of higher ODSAR underneath the transducer than on the wings (Fig. 3b). Although the strong ODSAR observed underneath the transducer indicates a high average strain, stronger Rabi oscillations on the wings indicate that the peak strain intensity is higher than under the transducer, consistent with the resonant behaviour of the device. Since the

https://doi.org/10.1038/s41928-023-01029-4

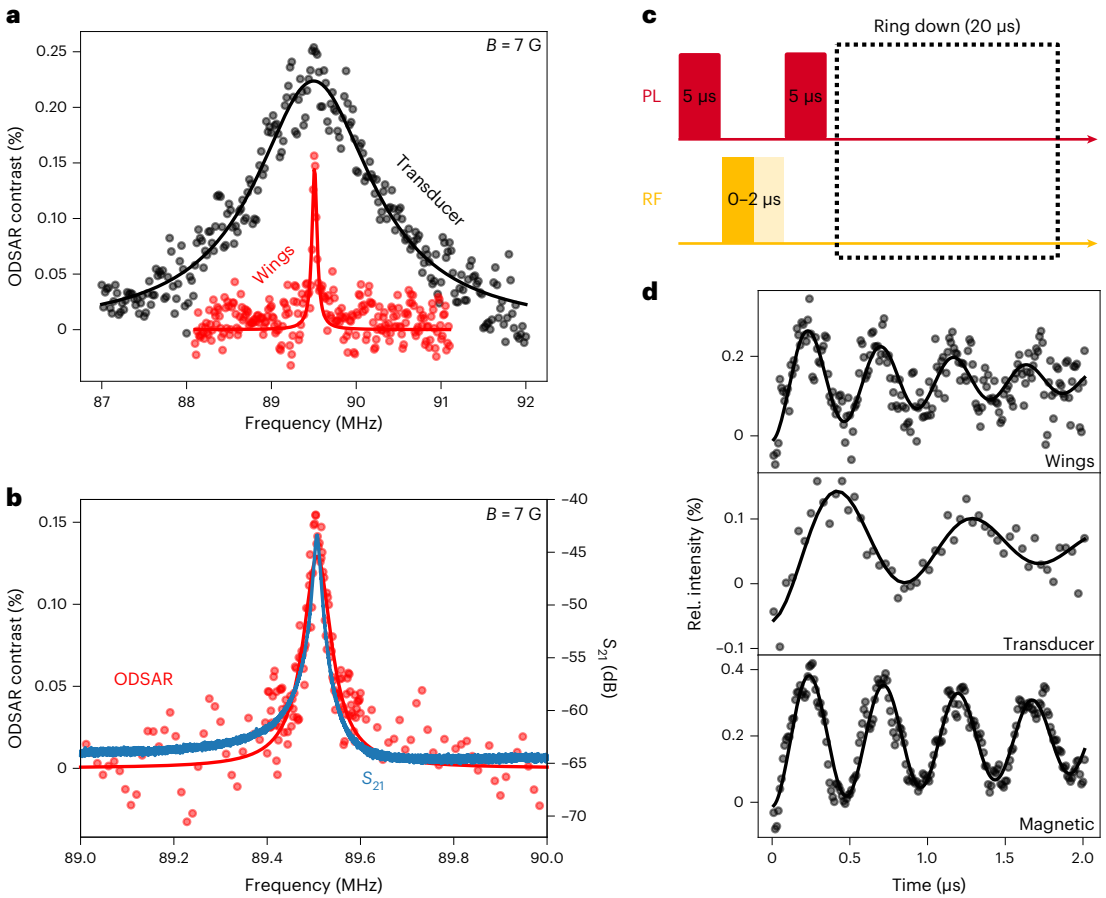

Fig. 4 | Coherent acoustic control measurements. a, Comparison of the ODSAR signals on the area of the device directly underneath the transducer (Transducer) and on the bulk of the resonator separated from the transducer (Wings). **b**, Comparison of high-resolution electrical measurement of *Q* and measurement of *Q* via the spin-acoustic resonance, showing effective filtering of spin resonance by the acoustic cavity. **c**, Pulse sequence used to measure coherent population oscillations followed by ring down of the shown acoustic cavity. RF, RF drive; PL, off-resonant PL readout laser. **d**, Rabi oscillations measured using an acoustically resonant RF drive (89.50 MHz) on the bulk of the resonator (Wings), an acoustically off-resonant RF drive that is still spin resonant (89.55 MHz) directly underneath the transducer (Transducer) and a spin-magnetic drive (89.50 MHz) from a closely placed RF antenna (Magnetic).

measurements of ODSAR and Rabi oscillations use a confocal volume that integrates over the depth of the resonator (10 µm), we can conclude that the total strain experienced underneath the transducer is higher, whereas the strain intensity on the wings is higher. Similarly, the faster decay in the acoustically driven oscillation compared with magnetically driven Rabi oscillations is attributable to the inhomogeneity in the acoustic strain distribution through the depth of our confocal slice. Although the frequency of the acoustic drive changes as the magnetic field remains constant, we expect this to have a negligible impact on the population oscillations as the detuning is small (50 kHz) relative to the homogeneous linewidth of the spin ensemble (2 MHz).

Conclusions

We have shown that bulk acoustic modes and $V_{\bar{Si}}$ can be acoustically coupled via spin-acoustic resonance, and have exploited this resonance to study the dynamical acoustic performance of a LOBAR. Our study finds that spins can be driven by both off-resonant forced oscillations and acoustic standing-wave resonance. An increased Rabi oscillation rate and filtered spin response highlights the benefit of using resonant elements in transduction schemes. The study is limited to ensemble measurements as a result of the naturally occurring $V_{\bar{Si}}$ in the high-purity semi-insulating 4H-SiC used, but a higher depth resolution can be achieved through layered ion implantation into a material with fewer intrinsic defects in the unimplanted material, useful for characterizing acoustic systems where strain is not concentrated near the surface of the device[29].

As a MEMS metrology technique, this could see application in monitoring the performance of accelerometers, gyroscopes and clocks over their lifetime and allows a fully depth-sensitive means of device characterization[30–32]. The identification of device tethers as a centre of stress concentration could contribute to improvements in *Q* via tether optimization[33]. Conversely, high-purity or isotopically purified material with a minimal ensemble density would also open studies of single-defect acoustic coupling as a demonstration for quantum information processing applications. Thinning devices to a smaller thickness could help increase acoustic coupling and enhance the rate of optical readout[34,35]. This experimental work also reinforces recent theoretical proposals suggesting $V_{\bar{Si}}$ as a potential candidate for hybrid quantum memories and a means of microwave–optical qubit transduction schemes in a future quantum network[36].

Methods

The LOBAR devices are made on a 500-µm-thick semi-insulating 4H-SiC wafer from Cree. The wafer is thinned down to 200 µm using chemical mechanical polishing, before it was sent to Plasma-Therm for AlN deposition. A Mo–AlN–Mo layer of 100 nm:1,000 nm:100 nm thickness is sputter deposited. The LOBAR is fabricated with a combination of dry and wet etching, with further details provided elsewhere[24]. FEM simulations are made using the COMSOL 5.6 Multiphysics package to simulate device performance. Spin measurements are performed at room temperature with a home-built confocal microscope (Supplementary

Fig. 6). The ensemble is excited by a 2 mW 865 nm external-cavity diode laser focused by a 0.9-numerical-aperture microscope objective onto the backside of the LOBAR device. Ensemble PL is collected by the same objective and filtered by a 900 nm dichroic, a 900 nm long-pass filter and a 1,000 nm short-pass filter before being focused onto a 50 µm pinhole and then collected by a single-photon avalanche diode detector. Free-space magnetic RF excitation is supplied by a 25 µm wire suspended nearby and acoustic RF excitation is applied through wire-bonded ground–signal–ground pads in a two-port differentially driven configuration. For ODSAR and ODMR, the input microwave power is 22 dBm, and for Rabi oscillation measurements, the input power is 32 dBm (Supplementary Information).

Data availability

The data that support the findings of this study are available via Zenodo at https://doi.org/10.5281/zenodo.8117273.

References

1. Maity, S. et al. Coherent acoustic control of a single silicon vacancy spin in diamond. *Nat. Commun.* **11**, 193 (2020).
2. Whiteley, S. J. et al. Spin-phonon interactions in silicon carbide addressed by Gaussian acoustics. *Nat. Phys.* **15**, 490–495 (2019).
3. MacQuarrie, E. R. et al. Coherent control of a nitrogen-vacancy center spin ensemble with a diamond mechanical resonator. *Optica* **2**, 233–238 (2015).
4. Hernández-Mínguez, A., Poshakinskiy, A., Hollenbach, M., Santos, P. & Astakhov, G. Anisotropic spin-acoustic resonance in silicon carbide at room temperature. *Phys. Rev. Lett.* **125**, 107702 (2020).
5. Lee, D., Lee, K. W., Cady, J. V., Ovartchaiyapong, P. & Jayich, A. C. B. Topical review: spins and mechanics in diamond. *J. Opt.* **19**, 033001 (2017).
6. Lukin, D. M. et al. 4H-silicon-carbide-on-insulator for integrated quantum and nonlinear photonics. *Nat. Photon.* **14**, 330–334 (2020).
7. Bracher, D. O., Zhang, X. & Hu, E. L. Selective Purcell enhancement of two closely linked zero-phonon transitions of a silicon carbide color center. *Proc. Natl Acad. Sci. USA* **114**, 4060–4065 (2017).
8. Wolfowicz, G., Whiteley, S. J. & Awschalom, D. D. Electrometry by optical charge conversion of deep defects in 4H-SiC. *Proc. Natl Acad. Sci. USA* **115**, 7879–7883 (2018).
9. Wang, C. et al. High-Q microresonators on 4H-silicon-carbide-on-insulator platform for nonlinear photonics. *Light Sci. Appl.* **10**, 139 (2021).
10. Soykal, O. O. & Reinecke, T. L. Quantum metrology with a single spin-3/2 defect in silicon carbide. *Phys. Rev. B* **95**, 081405 (2017).
11. Udvarhelyi, P. & Gali, A. Ab initio spin-strain coupling parameters of divacancy qubits in silicon carbide. *Phys. Rev. Appl.* **10**, 054010 (2018).
12. Schirhagl, R., Chang, K., Loretz, M. & Degen, C. L. Nitrogen-vacancy centers in diamond: nanoscale sensors for physics and biology. *Annu. Rev. Phys. Chem.* **65**, 83–105 (2014).
13. Xie, Q. et al. Imaging gigahertz zero-group-velocity Lamb waves. *Nat. Commun.* **10**, 2228 (2019).
14. Whiteley, S. J., Heremans, F. J., Wolfowicz, G., Awschalom, D. D. & Holt, M. V. Correlating dynamic strain and photoluminescence of solid-state defects with stroboscopic X-ray diffraction microscopy. *Nat. Commun.* **10**, 3386 (2019).
15. Chandrahalim, H. et al. Heterodyne laser-Doppler interferometric characterization of contour-mode resonators above 1 GHz. In *2009 IEEE International Ultrasonics Symposium* 1044–1049 (IEEE, 2009).
16. Riedel, D. et al. Resonant addressing and manipulation of silicon vacancy qubits in silicon carbide. *Phys. Rev. Lett.* **109**, 226402 (2012).
17. Nagy, R. et al. Quantum properties of dichroic silicon vacancies in silicon carbide. *Phys. Rev. Appl.* **9**, 034022 (2018).
18. Nagy, R. et al. High-fidelity spin and optical control of single silicon-vacancy centres in silicon carbide. *Nat. Commun.* **10**, 1954 (2019).
19. Hernández-Mínguez, A., Poshakinskiy, A. V., Hollenbach, M., Santos, P. V. & Astakhov, G. V. Acoustically induced coherent spin trapping. *Sci. Adv.* **7**, eabj5030 (2021).
20. Flannery, C. M. & von Kiedrowski, H. Effects of surface roughness on surface acoustic wave propagation in semiconductor materials. *Ultrasonics* **40**, 83–87 (2002).
21. Rosskopf, T. et al. Investigation of surface magnetic noise by shallow spins in diamond. *Phys. Rev. Lett.* **112**, 147602 (2014).
22. Chen, H. Y., Bhave, S. A. & Fuchs, G. D. Acoustically driving the single-quantum spin transition of diamond nitrogen-vacancy centers. *Phys. Rev. Appl.* **13**, 054068 (2020).
23. Gong, S., Kuo, N.-K. & Piazza, G. A 1.75 GHz piezoelectrically-transduced SiC lateral overmoded bulk acoustic-wave resonator. In *2011 16th International Solid-State Sensors, Actuators and Microsystems Conference* 922–925 (IEEE, 2011).
24. Jiang, B., Opondo, N. P. & Bhave, S. A. Semi-insulating 4H-SiC lateral bulk acoustic wave resonators. *Appl. Phys. Lett.* **118**, 114002 (2021).
25. Udvarhelyi, P., Shkolnikov, V. O., Gali, A., Burkard, G. & Pályi, A. Spin-strain interaction in nitrogen-vacancy centers in diamond. *Phys. Rev. B* **98**, 075201 (2018).
26. Poshakinskiy, A. V. & Astakhov, G. V. Optically detected spin-mechanical resonance in silicon carbide membranes. *Phys. Rev. B* **100**, 094104 (2019).
27. Jo, B., Ghatge, M. & Tabrizian, R. d_{15}-enhanced shear-extensional aluminum nitride resonators with $k^2t > 4.4\%$ for wide-band filters. In *2017 19th International Conference on Solid-State Sensors, Actuators and Microsystems (TRANSDUCERS)* 94–97 (IEEE, 2017).
28. Maity, S. et al. Mechanical control of a single nuclear spin. *Phys. Rev. X* **12**, 011056 (2022).
29. Kasper, C. et al. Influence of irradiation on defect spin coherence in silicon carbide. *Phys. Rev. Appl.* **13**, 044054 (2020).
30. Zhai, Y. et al. Design, fabrication and test of a bulk SiC MEMS accelerometer. *Microelectron. Eng.* **260**, 111793 (2022).
31. Hamelin, B., Yang, J., Liu, Z. & Ayazi, F. Monocrystalline 4H silicon carbide-on-insulator substrates for Nav-grade planar BAW gyroscopes. In *2021 IEEE International Symposium on Inertial Sensors and Systems (INERTIAL)* 1–4 (IEEE, 2021).
32. Gosavi, T. A., MacQuarrie, E. R., Fuchs, G. D. & Bhave, S. A. HBAR as a high frequency high stress generator. In *2015 IEEE International Ultrasonics Symposium (IUS)* 1–4 (IEEE, 2015).
33. Hamelin, B., Yang, J., Daruwalla, A., Wen, H. & Ayazi, F. Monocrystalline silicon carbide disk resonators on phononic crystals with ultra-low dissipation bulk acoustic wave modes. *Sci. Rep.* **9**, 18698 (2019).
34. Ziaei-Moayyed, M., Habermehl, S., Branch, D., Clews, P. J. & Olsson, R. H. Silicon carbide lateral overtone bulk acoustic resonator with ultrahigh quality factor. In *2011 IEEE 24th International Conference on Micro Electro Mechanical Systems* 788–792 (IEEE, 2011).
35. Dietz, J. R. & Hu, E. L. Optical and strain stabilization of point defects in silicon carbide. *Appl. Phys. Lett.* **120**, 184001 (2022).
36. Raniwala, H., Krastanov, S., Eichenfield, M. & Englund, D. A spin-optomechanical quantum interface enabled by an ultrasmall mechanical and optical mode volume cavity. Preprint at *arXiv* https://doi.org/10.48550/arXiv.2202.06999 (2022).

Acknowledgements
The research was supported by NSF RAISE-TAQS Award 1839164. A.M.D. acknowledges support from the Science and Technology Center for Integrated Quantum Materials, National Science Foundation (NSF), grant DMR-1231319. The SiC resonators were fabricated in the Birck Nanotechnology Center at Purdue University. Chemical mechanical polishing was completed at NOVASiC and AlN deposition was performed by Plasma-Therm. We thank O. Soykal for helpful discussions.

Author contributions
J.R.D., B.J., A.M.D., S.A.B. and E.L.H. conceived the experiment and contributed to designing of the measurements. B.J. simulated, designed and fabricated the acoustic resonators. J.R.D. and A.M.D. packaged, electrically characterized and performed the electron microscopy measurements of the devices. J.R.D. performed the spin resonance and acoustic metrology measurements with assistance from A.M.D. J.R.D., B.J. and A.M.D. analysed the data and prepared the figures included in the manuscript. J.R.D. wrote the manuscript. All authors commented and provided inputs on the final manuscript.

Competing interests
The authors declare no competing interests.

Additional information
Supplementary information The online version contains supplementary material available at https://doi.org/10.1038/s41928-023-01029-4.

Correspondence and requests for materials should be addressed to Sunil A. Bhave.

Peer review information *Nature Electronics* thanks Paulo Santos and the other, anonymous, reviewer(s) for their contribution to the peer review of this work.

Reprints and permissions information is available at www.nature.com/reprints.

Publisher's note Springer Nature remains neutral with regard to jurisdictional claims in published maps and institutional affiliations.

Open Access This article is licensed under a Creative Commons Attribution 4.0 International License, which permits use, sharing, adaptation, distribution and reproduction in any medium or format, as long as you give appropriate credit to the original author(s) and the source, provide a link to the Creative Commons license, and indicate if changes were made. The images or other third party material in this article are included in the article's Creative Commons license, unless indicated otherwise in a credit line to the material. If material is not included in the article's Creative Commons license and your intended use is not permitted by statutory regulation or exceeds the permitted use, you will need to obtain permission directly from the copyright holder. To view a copy of this license, visit http://creativecommons.org/licenses/by/4.0/.

© The Author(s) 2023